Phytochemical-Guided Green Synthesis of Structurally Defined ZnO Nanoparticles from Butea monosperma Root Extract and Their Antibacterial Potential

Rajeshreeba A. Jadeja
Marwadi University
Suranjana V. Mayani
suranjana.mayani@marwadieducation.edu.in

Marwadi University https://orcid.org/0000-0002-2624-3305

Research Article

Keywords: Green synthesis, Zinc oxide nanoparticles, Butea monosperma root extract, Phytochemical-mediated synthesis, antimicrobial activity, PXRD characterization

Posted Date: April 17th, 2026

DOI: https://doi.org/10.21203/rs.3.rs-9057029/v1

Phytochemical-Guided Green Synthesis of Structurally Defined ZnO Nanoparticles from *Butea monosperma* Root Extract and Their Antibacterial Potential

Rajeshreeba A. Jadeja[1], Suranjana V. Mayani[1*]

[1]Department of Chemistry, Marwadi University, Rajkot-Morbi Road, P.O. Gauridad, Rajkot 360003, Gujarat, India, E mail: rajeshreeba.jadeja129444@marwadiuniversity.ac.in, Tel: +91-9512501125, ORCID: 0009-0002-2940-1820

[1*]Department of Chemistry, Faculty of Science, Marwadi University, Rajkot-Morbi Road, P.O. Gauridad, Rajkot 360003, Gujarat, India, E mail: suranjana.mayani@marwadieducation.edu.in, Tel: +91-9979980770, ORCID: 0000-0002-2624-3305

Abstract

Green synthesis of metal oxide nanoparticles using plant-derived phytochemicals represents a sustainable and surface-engineered approach for developing functional nanomaterials. In the present study, an aqueous root extract of *Butea monosperma* was employed as a bio reducing and stabilizing agent for the synthesis of zinc oxide nanoparticles (ZnO NPs). Phytochemical profiling using qualitative assays, thin-layer chromatography (TLC), high-performance liquid chromatography (HPLC), and LC–MS confirmed the presence of polyphenols, flavonoids, tannins, and triterpenoids, which are known to facilitate metal ion reduction and nanoparticle stabilization. UV–visible spectroscopy revealed a characteristic absorption edge in the UV region with an optical band gap of 3.69 eV, indicating nanoscale ZnO formation. Powder X-ray diffraction (PXRD) confirmed the formation of crystalline hexagonal wurtzite ZnO (JCPDS No. 36-1451) with an average crystallite size of 12–18 nm. Dynamic light scattering analysis showed a hydrodynamic diameter of 255.8 nm with a polydispersity index of 0.389, while a negative zeta potential (–25 mV) indicated moderate colloidal stability due to phytochemical surface capping. FTIR spectra demonstrated the involvement of hydroxyl and carbonyl functional groups in nanoparticle formation. SEM–EDX analysis confirmed nanoscale morphology and elemental purity (Zn 74.48 wt%, O 25.52 wt%). The synthesized ZnO NPs exhibited concentration-dependent antibacterial activity, with a maximum inhibition zone of 20 mm against *Bacillus* sp. and 15 mm against *Escherichia coli* at 1000 µg/mL. These findings establish a direct correlation between root phytochemical composition, nanoparticle physicochemical properties, and antimicrobial performance, demonstrating the potential of *B. monosperma*-mediated ZnO NPs as phytochemical-engineered antibacterial nanomaterials.

Keywords: - Green synthesis, Zinc oxide nanoparticles, Butea monosperma root extract, Phytochemical-mediated synthesis, antimicrobial activity, PXRD characterization

Graphical abstract: -

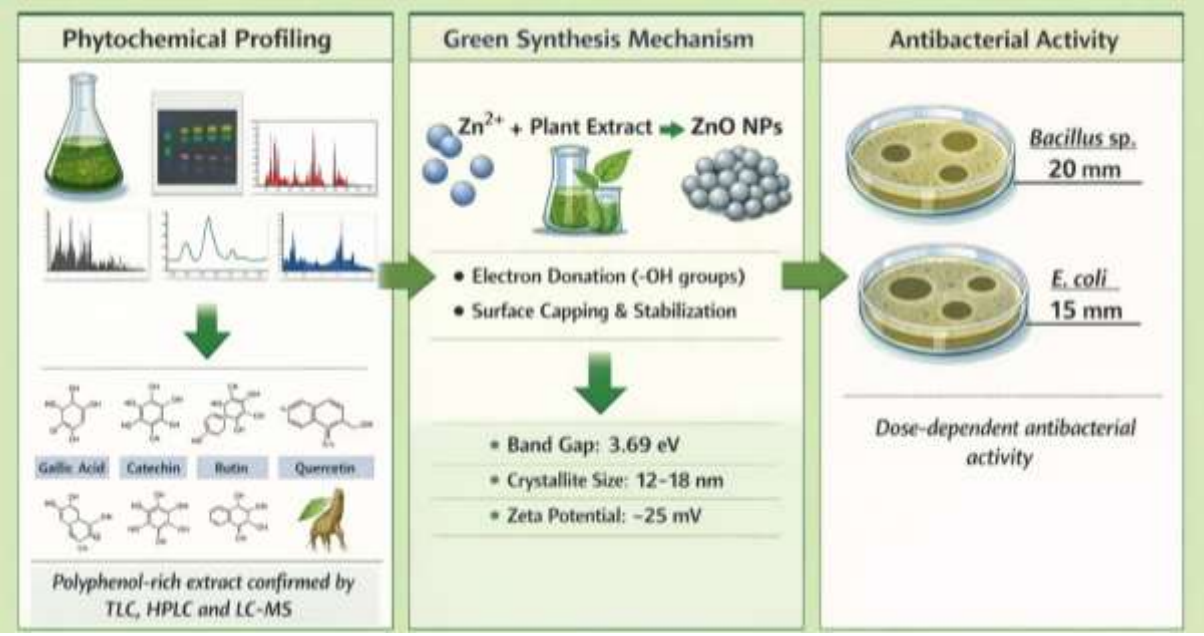

1. Introduction

The development of environmentally benign nanomaterial synthesis strategies has become a major focus in green nanotechnology [1]. Conventional chemical and physical methods for synthesizing metal oxide nanoparticles often involve toxic reagents, high energy consumption, and hazardous by-products [2]. In contrast, plant-mediated synthesis provides a sustainable alternative by utilizing naturally occurring phytochemicals as reducing and stabilizing agents [3]. Bioactive metabolites such as flavonoids, phenolic acids, tannins, terpenoids, and alkaloids possess functional groups capable of donating electrons, chelating metal ions, and stabilizing nucleating nanostructures [4]. This dual functionality enables controlled nanoparticle formation under mild conditions without requiring toxic additives. Zinc oxide nanoparticles (ZnO NPs) have attracted considerable attention due to their wide band gap (~3.3 eV in bulk form), high exciton binding energy, chemical stability, and multifunctional applications in biomedicine, catalysis, antimicrobial coatings, and surface-engineered materials [5]. At the nanoscale, ZnO exhibits enhanced surface area and increased generation of reactive oxygen species (ROS), contributing to its antibacterial activity through membrane disruption, oxidative stress induction, and Zn^{2+} ion release [6]. The physicochemical characteristics of ZnO NPs—including crystallite size, morphology, surface charge, and band gap strongly influence their biological performance. Although plant-mediated ZnO synthesis has been widely reported, limited studies correlate detailed phytochemical fingerprinting (TLC–HPLC–LC–MS) with

nanoparticle crystallinity, surface charge, and antimicrobial performance [7]. Furthermore, root-derived phytochemicals remain chemically underexplored compared to leaves, bark, or flowers, despite their distinct secondary metabolite composition [8]. Establishing a direct relationship between phytochemical profile and nanoparticle properties remains an important research gap in green nanoscience [9]. In this context, the present investigation was designed to systematically explore the phytochemical composition of *Butea monosperma* root extract through qualitative screening and advanced chromatographic techniques including TLC, HPLC, and LC–MS, followed by its application in the green synthesis of zinc oxide nanoparticles [10]. Furthermore, the study sought to establish a clear relationship between the identified bioactive constituents and the resulting nanoparticle characteristics, with particular emphasis on crystallinity, surface properties, physicochemical behaviour, and antibacterial efficacy [11]. A schematic representation of the overall experimental approach is illustrated in **Fig. 1.**

2. Materials and Methods

2.1 Plant Material

Fresh roots of *Butea monosperma* (Fabaceae) were collected from Ranavav, Gujarat, India, in September 2025. The roots were thoroughly washed, shade-dried at ambient temperature for four weeks, and pulverized into a fine powder using a laboratory mill [12].

2.2 Extraction Procedure

Ten grams of powdered root material were subjected to Soxhlet extraction using 100 mL distilled water at 95–100 °C for 16 h. The extract was filtered through Whatman No. 1 filter paper and concentrated under reduced pressure using a rotary evaporator [13]. The dried extract was weighed, and extraction yield (%) was calculated as:

$$\text{Yield (\%)} = \frac{2}{10} \times 100$$

$$\text{Yield (\%)} = 20\%$$

The concentrated extract was stored at 4 °C until further use.

2.3 Qualitative Phytochemical Screening

Standard phytochemical tests were performed to detect tannins, flavonoids, alkaloids, saponins, and steroids using established protocols. Colorimetric and precipitation reactions were recorded as indicators of the presence of respective secondary metabolites [14].

2.4 Thin-Layer Chromatography (TLC)

TLC analysis was carried out using pre-coated silica gel 60 F_{254} plates (0.2 mm thickness). The extract was applied using a microcapillary syringe. Plates were developed in optimized solvent systems specific to phytochemical classes. The development chamber was pre-saturated for 30 min prior to use. Developed plates were visualized under UV light (254 and 365 nm) followed by post-derivatization using $AlCl_3$, $FeCl_3$, PEG, and Dragendorff's reagents. Rf values were calculated and documented [15].

2.5 High-Performance Liquid Chromatography (HPLC) Analysis

HPLC analysis was performed using a Shimadzu LC-20AT system equipped with a UV detector. Separation was achieved using a reverse-phase C18 column (250 × 4.6 mm, 5 µm) maintained at 30 °C. The mobile phase consisted of solvent A (0.1% formic acid in water) and solvent B (0.1% formic acid in acetonitrile) with gradient elution (5–95% B over 30 min). The flow rate was 1.0 mL/min, injection volume was 20 µL, and detection wavelength was set at 280 nm based on polyphenolic absorbance maxima [16].

2.6 LC–MS Analysis

LC–MS analysis was conducted using a Waters Acquity UPLC system coupled with an electrospray ionization (ESI) mass spectrometer operating in positive and negative ion modes. Chromatographic separation was performed on a reverse-phase C18 column using the same solvent system as HPLC. The scan range was m/z 100–1000. Capillary voltage, source temperature, and cone voltage were optimized for compound detection. Tentative compound identification was performed by comparing m/z values with standard databases [17].

2.7 Green Synthesis of Zinc oxide Nanoparticles (ZnO NPs)

A 0.1 M zinc acetate dihydrate solution was prepared in distilled water. Equal volumes (50 mL each) of zinc acetate solution and root extract were mixed under continuous magnetic stirring (500 rpm) at 60 °C. A 2.0 M NaOH solution was added dropwise until pH 10–12 was achieved. The reaction mixture was stirred for 1 h to ensure complete nucleation. The precipitate was collected by centrifugation (5000 rpm, 15 min), washed thrice with distilled water and methanol, and dried at 60 °C. The dried precursor was calcined at 450 °C for 2 h to obtain crystalline ZnO nanoparticles [18].

2.8 Characterization of ZnO NPs

UV–Vis spectra were recorded between 200–800 nm. The absorption coefficient was calculated using the Beer–Lambert law, and the optical band gap was determined using the Tauc equation:

$$(\alpha h\nu)^2 = B(h\nu - E_g)$$

- DLS and zeta potential measurements were performed using a Malvern Zetasizer Nano ZS at 25 °C with a 173° backscatter detection angle.
- PXRD analysis was conducted using Cu Kα radiation (λ = 1.5406 Å). Crystallite size was calculated using the Debye–Scherrer equation:

$$D = \frac{K\lambda}{\beta \cos\theta}$$

- SEM–EDX analysis was performed to examine morphology and elemental composition [19].

2.9 Statistical Analysis

All experiments were performed in triplicate, and results were expressed as mean ± standard deviation. Statistical significance was evaluated using one-way ANOVA followed by Tukey's post hoc test, with $p < 0.05$ considered statistically significant [20].

3. Results and Discussion

3.1 Phytochemical Profiling

Qualitative Phytochemical Analysis

Preliminary phytochemical screening of the aqueous root extract of *Butea monosperma* revealed the presence of multiple bioactive secondary metabolites, including alkaloids, flavonoids, phenolics, tannins, saponins, and triterpenoids [21]. Characteristic colorimetric changes and precipitate formation observed during standard qualitative assays confirmed their presence. The detection of these metabolite classes is consistent with previous reports on *B. monosperma* and other members of the Fabaceae family. The abundance of polyphenolic constituents suggests strong redox potential, supporting the extract's suitability for nanoparticle biosynthesis through reduction and stabilization mechanisms [22]. The qualitative phytochemical constituents detected in the aqueous root extract are summarized in Table **1.**

Table 1 Qualitative phytochemical constituents detected in aqueous root extract of Butea monosperma.

Phytochemical class	Test performed	Observation	Result
Alkaloids	Dragendorff's	Orange precipitate	+
Flavonoids	Shinoda test	Pink/red coloration	+
Phenolics	Ferric chloride test	Blue-green coloration	+
Tannins	Lead acetate test	White precipitate	+
Saponins	Foam test	Persistent froth	+
Triterpenoids	Liebermann-Burchard test	Green coloration	+

3.2 Thin-Layer Chromatography (TLC)

TLC analysis provided a distinct phytochemical fingerprint of the aqueous root extract. Under UV illumination (254 and 366 nm) and after derivatization, multiple well-resolved bands were observed, confirming chemical diversity. Flavonoids produced intense yellow-green fluorescence following $AlCl_3$ and NaOH spraying, with Rf values ranging from 0.20 to 0.82, indicating compounds of varying polarity [23]. Phenolic compounds visualized with $FeCl_3$ reagent displayed blue–black bands (Rf 0.18–0.72), characteristic of hydroxylated aromatic structures. Dragendorff's reagent revealed orange-brown spots (Rf 0.20, 0.40, 0.65), confirming the presence of alkaloids. Tannin-specific solvent systems produced greenish-blue bands, indicating both hydrolysable and condensed tannins. Overall, the TLC profile confirms a chemically complex extract dominated by flavonoids and polyphenols. This chromatographic fingerprint provides a reproducible reference for phytochemical standardization and supports subsequent HPLC and LC–MS analyses [24]. The TLC chromatograms under UV illumination are shown in the supplementary file and the detailed Rf values and solvent systems are summarized in **Table S1-S1.6** in the supplementary file.

3.3 High performance liquid chromatography (HPLC)

The HPLC chromatogram demonstrated a phytochemically rich profile characterized by multiple well-defined peaks. A dominant peak at RT 12.669 min accounted for 64.7% of total peak area, suggesting a major flavonoid or phenolic constituent. A second prominent peak at RT 17.007 min represented 21.5% of the area, while several minor peaks (RT 12.998–20.276 min) indicated additional secondary metabolites. The predominance of two major peaks suggests that specific flavonoid glycosides or phenolic acids constitute the principal phytochemical fraction. These chromatographic findings align with TLC results and correlate with LC–MS tentative identifications,

confirming the extract's polyphenolic richness. The high abundance of hydroxylated compounds provides mechanistic support for their involvement in Zn^{2+} reduction and nanoparticle stabilization [25]. The HPLC chromatogram of the root extract is shown in **Fig. 2.**

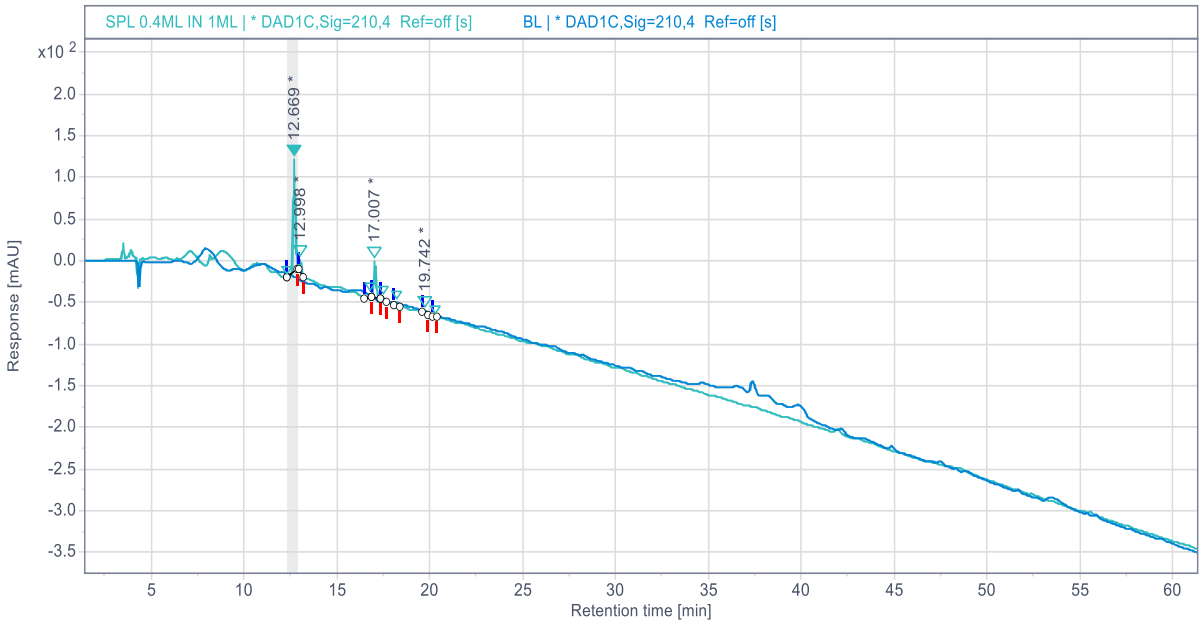

3.4 LC–MS Phytochemical Fingerprinting

LC–MS analysis enabled tentative identification of major bioactive compounds. Prominent signals were observed at retention times between 15–33 min with characteristic m/z values corresponding to:

- **Gallic acid** (m/z ~169–170)
- **Catechin/Epicatechin** (m/z ~289–290)
- **Quercetin derivatives** (m/z ~301–303)
- **Rutin** (m/z ~609–610)
- **Lupeol** (m/z ~426)

These metabolites are rich in hydroxyl and carbonyl functional groups, facilitating electron donation for Zn^{2+} reduction. Polyphenols such as catechin, quercetin, and rutin likely act as both reducing and capping agents through chelation and hydrogen bonding. Triterpenoids such as lupeol contribute steric stabilization via hydrophobic interactions [26]. Collectively, LC–MS Identifications were tentative based on mass database comparison that the aqueous root extract contains redox-active metabolites capable of mediating controlled nucleation and growth of ZnO nanoparticles [27]. The LC–MS spectrum used for phytochemical identification is presented in **Fig. 3.**

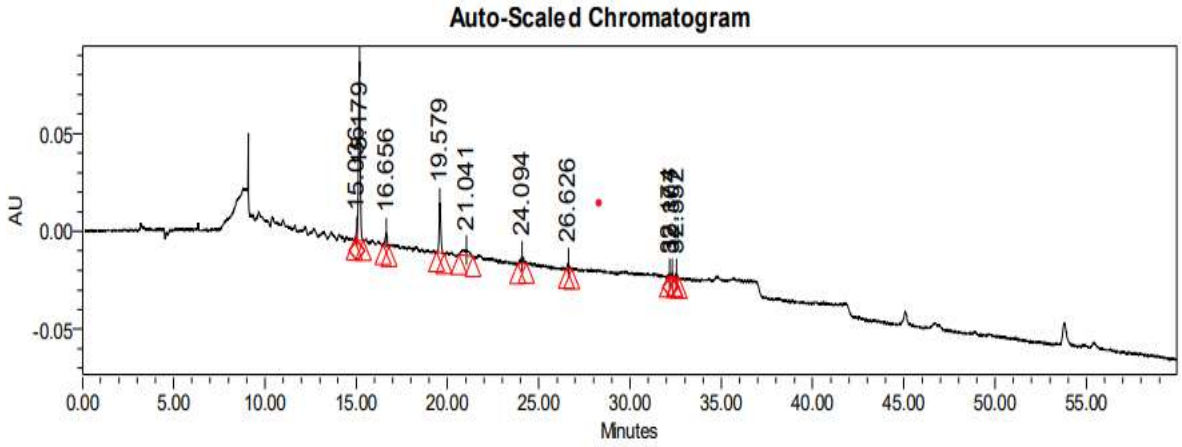

3.5 Green Synthesis of ZnO Nanoparticles

Upon mixing zinc acetate with the root extract, the solution changed from colourless to yellowish-brown, indicating nanoparticle formation. This visual transition reflects phytochemical-mediated reduction of Zn^{2+} ions and subsequent nucleation of ZnO nanocrystals. After centrifugation and calcination at 450 °C, approximately 0.27 g of ZnO nanoparticles were obtained per batch. The successful yield demonstrates the efficiency of the plant-mediated synthetic route compared to conventional chemical methods [28].

3.6 UV–Visible Spectroscopy and Band Gap Analysis

The UV–visible spectrum of the synthesized ZnO nanoparticles exhibited a characteristic absorption maximum at **365 nm**, corresponding to the intrinsic band-gap absorption of ZnO arising from electron transitions between the valence band and conduction band. The optical band gap was estimated using the **Tauc relation for direct allowed**

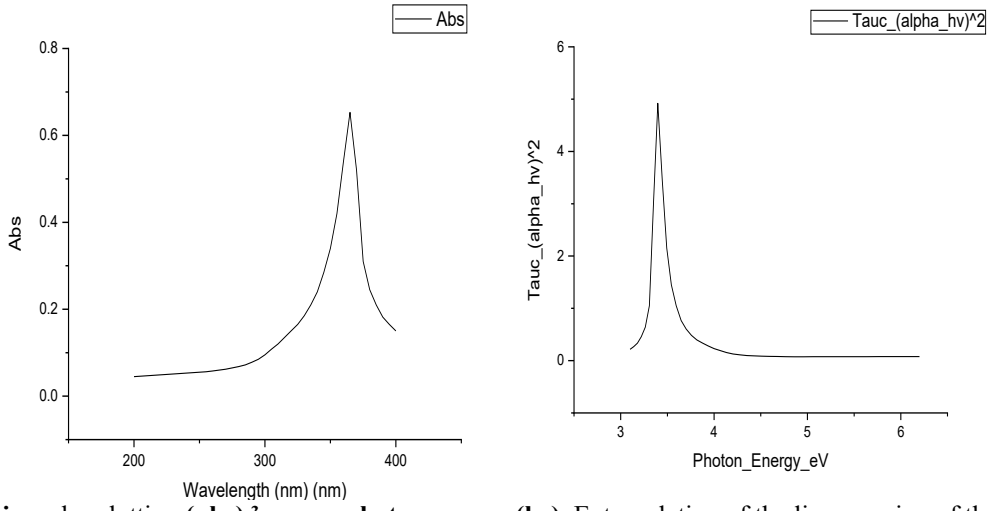

transitions, by plotting **(αhν) ² versus photon energy (hν)**. Extrapolation of the linear region of the Tauc plot to the energy axis yielded a band gap of approximately **3.69 eV**, which is slightly higher than bulk ZnO (3.3 eV),

indicating the nanoscale nature of the synthesized particles [29]. The UV–Vis absorption spectrum and corresponding Tauc plot are shown in **Fig. 4.**

3.7 FTIR Analysis

FTIR spectra revealed functional groups involved in nanoparticle synthesis. A broad band at ~3364 cm^{-1} corresponds to O–H stretching of polyphenols. Peaks at 1640 cm^{-1} (C=O stretching), 1384 cm^{-1} (C–O bending), and 1064 cm^{-1} (C–O–C stretching) indicate carbonyl and ether functionalities. Importantly, characteristic Zn–O stretching vibrations were observed at 620 cm^{-1}, confirming ZnO formation. Peak shifts and intensity variations after synthesis indicate phytochemical binding to nanoparticle surfaces, supporting their stabilizing role [30]. The FTIR spectrum of ZnO nanoparticles is presented in **Fig. 5.** The detailed FTIR band assignments corresponding to functional groups are presented in **Table 2.**

Table 2 FTIR band assignments of Butea monosperma root extract-mediated ZnO nanoparticles.

Wavenumber (cm-1)	Functional group	Tentative assignment
3400	O-H stretching	Phenolic, flavonoids
1640	C=O stretching	Carbonyl compounds
1384	C-O bending	Polyphenolic
1040	C-O-C stretching	Ether linkage
620	Zn-Stretching	ZnO vibration mode

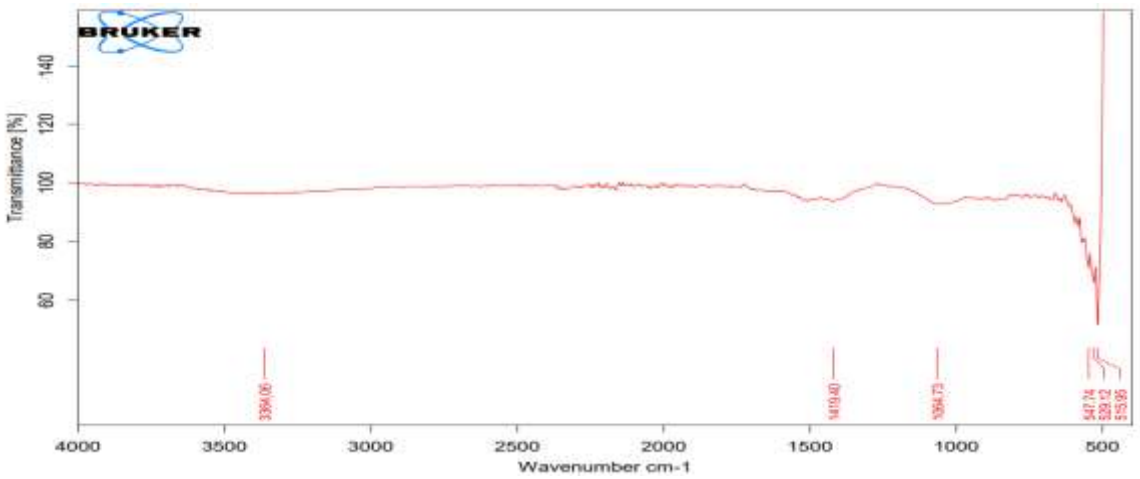

3.8 Zeta Potential and Particle Size

Dynamic light scattering analysis showed a Z-average hydrodynamic diameter of **255.8 nm** with a polydispersity index (PDI) of **0.389**, indicating moderate size distribution typical of plant-mediated nanoparticles. The intensity peak centered around 206 nm. Zeta potential analysis revealed a surface charge of **–25 mV**, suggesting moderate colloidal stability. The negative surface charge is attributed to adsorption of polyphenolic groups, which generate electrostatic repulsion and prevent excessive aggregation [31].

3.9 SEM–EDX

SEM micrographs revealed irregular, polydisperse, and partially agglomerated nanoparticles forming porous microstructures. Agglomeration is commonly observed in biosynthesized nanoparticles due to phytochemical surface interactions. EDX analysis confirmed elemental composition with Zn (74.48 wt%) and O (25.52 wt%), consistent with stoichiometric ZnO. The absence of significant impurity peaks confirms high purity of the synthesized nanoparticles [32]. The morphology and elemental composition of ZnO nanoparticles are shown in **Fig. 6.** The elemental composition obtained from EDX analysis is summarized in **Table 3.**

Table 3 *Elemental composition of green-synthesized ZnO nanoparticles determined by EDX analysis.*

Elements	**Line type**	**Wt%**	**Atomic %**	
Zn	K Series	74.48	41.67	
O	K Series		25.52	58.33

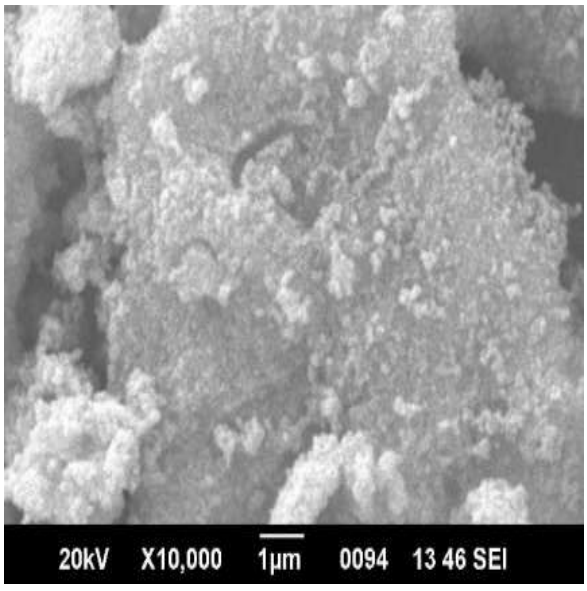

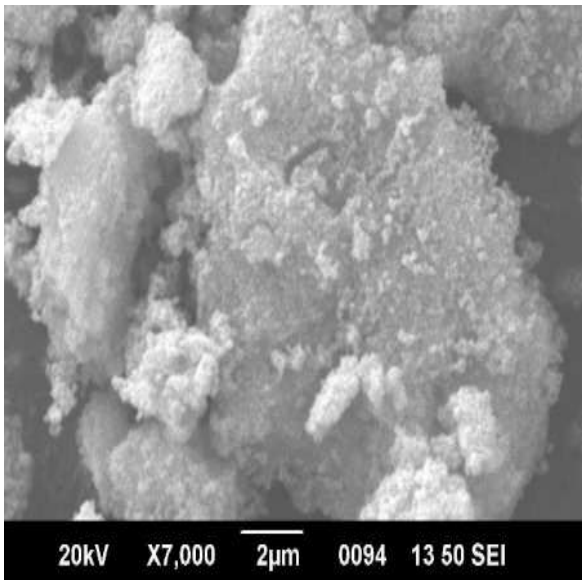

3.10 PXRD

PXRD patterns showed diffraction peaks at 2θ values of 31.88°, 34.51°, 36.36°, 47.68°, 56.74°, and 62.99°, corresponding to (100), (002), (101), (102), (110), and (103) planes of hexagonal wurtzite ZnO (JCPDS No. 36-1451). No secondary phase peaks were detected, confirming phase purity. Scherrer equation calculations estimated crystallite size between **12–18 nm**, validating nanoscale crystalline formation [33]. The PXRD pattern confirming the crystalline structure of ZnO nanoparticles is shown in **Fig. 7.**

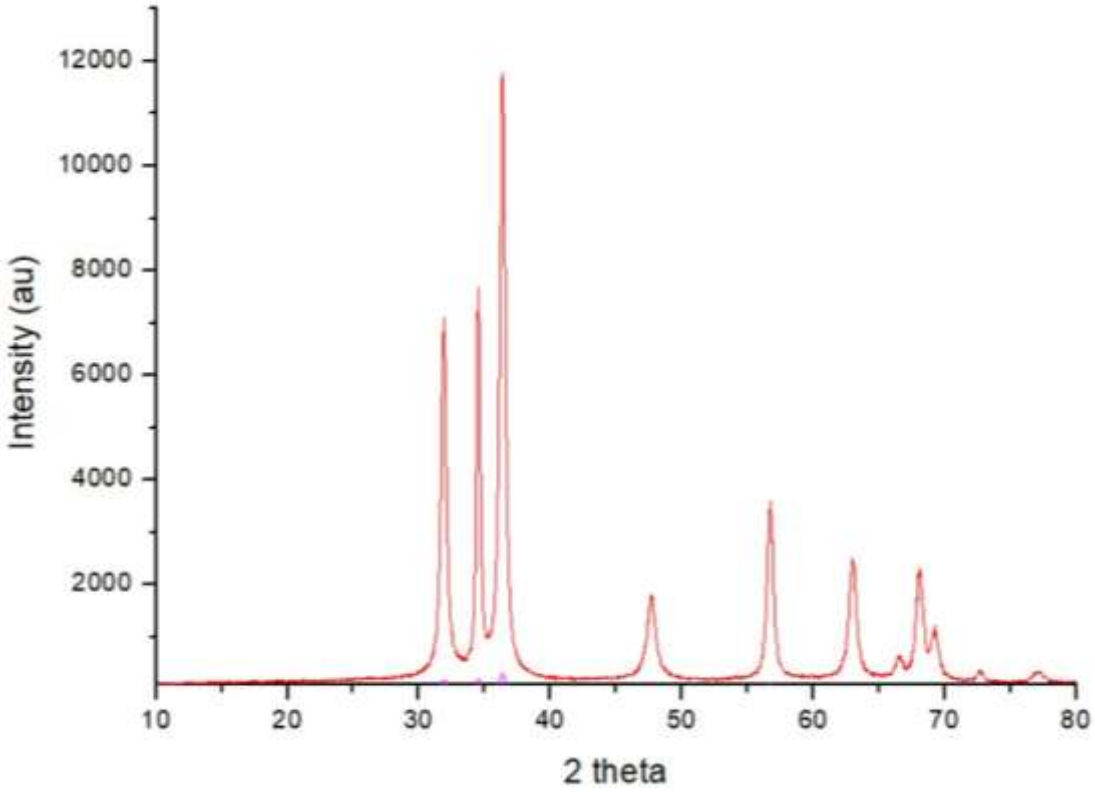

3.11 Proposed Phytochemical-Mediated Mechanism

Polyphenolic compounds donate electrons via hydroxyl and carbonyl groups, reducing Zn^{2+} ions to ZnO nuclei. Simultaneously, tannins, flavonoids, and saponins adsorb onto nanoparticle surfaces, providing steric and electrostatic stabilization. This dual functionality ensures controlled nucleation, moderated growth, and colloidal stability of ZnO nanoparticles synthesized via the green route [34].

3.12 Antimicrobial Activity of ZnO Nanoparticles

ZnO nanoparticles exhibited concentration-dependent antibacterial activity against *Escherichia coli (E. coli)* and Bacillus sp. using agar well diffusion assays.

At 1000 µg/mL, the maximum zone of inhibition was:

- 20 mm against *Bacillus sp.*
- 15 mm against *Escherichia coli (E. coli)*

No inhibition was observed for *Escherichia coli (E. coli)* at lower concentrations (250 and 500 µg/mL). *Bacillus sp.* demonstrated higher susceptibility, likely due to differences in cell wall structure between Gram-positive and Gram-negative bacteria [35].

The enhanced antibacterial effect may be attributed to:

- Reactive oxygen species (ROS) generation
- Zn^{2+} ion release
- Membrane disruption
- High surface area associated with 12–18 nm crystallite size

These findings confirm that phytochemical-mediated ZnO nanoparticles are structurally defined and biologically active, supporting their potential application as sustainable antimicrobial nanomaterials. All values represent mean ± SD (n = 3) [36]. Representative antibacterial activity plates are shown in **Fig. 8.** The quantitative zone of inhibition values at different concentrations are presented in **Table 4.** The concentration-dependent antibacterial activity is further illustrated in **Fig. 9.**

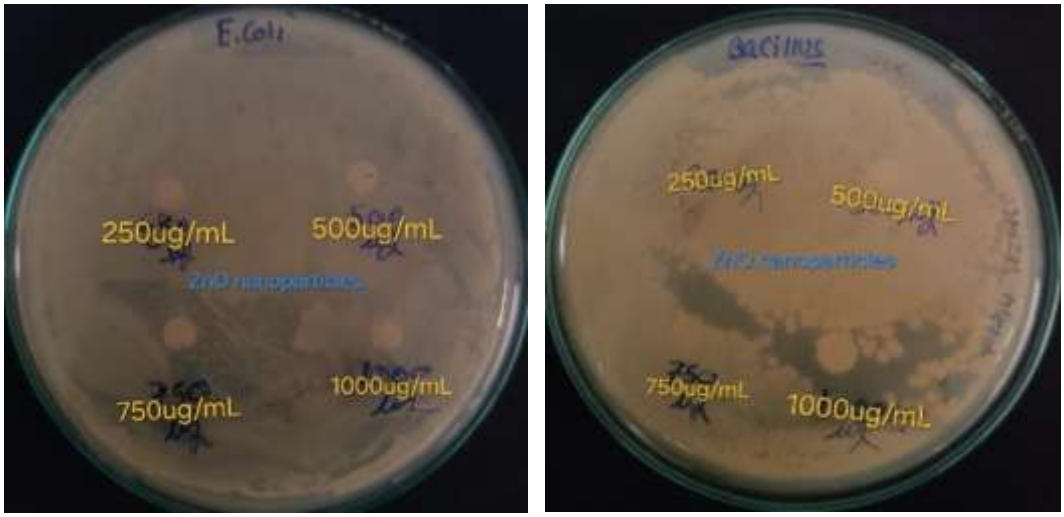

Escherichia coli (E. coli) Bacillus sp.

Table 4 Zone of inhibition (mm) ZnO nanoparticles against tested bacterial strains at different concentrations

Microorganism	**Concentrations µg/mL**	**Zone of inhibition (mm)***
Escherichia coli (E. coli)	250	Not detected
	500	Not detected
	750	10
	1000	15
Bacillus sp.	250	1
	500	5
	750	10
	1000	20

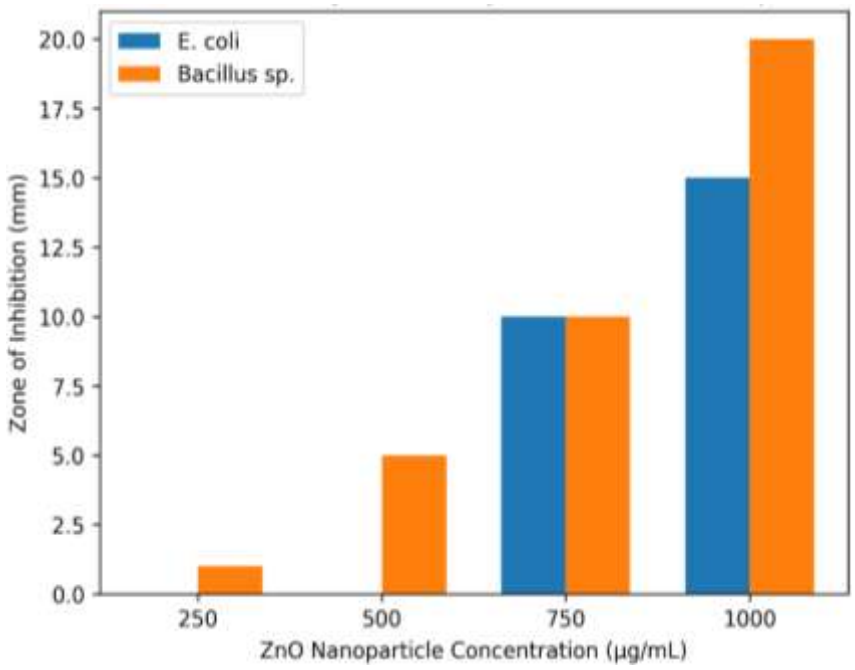

4. Conclusion and Future Perspectives

This study successfully demonstrated a comprehensive phytochemical investigation and green synthesis strategy utilizing aqueous root extract of *Butea monosperma* for the fabrication of zinc oxide nanoparticles (ZnO NPs). Chromatographic and spectrometric analyses (TLC, HPLC, and LC–MS) confirmed the presence of polyphenolic and bioactive metabolites including gallic acid, catechin, epicatechin, rutin, quercetin derivatives, and lupeol, which functioned synergistically as natural reducing and stabilizing agents during nanoparticle formation. The biosynthesized ZnO NPs exhibited a characteristic UV absorption band with an optical band gap of 3.69 eV, indicating nanoscale quantum confinement effects. PXRD analysis confirmed a crystalline hexagonal wurtzite

structure with an estimated crystallite size of 12–18 nm, while FTIR spectra verified phytochemical-mediated surface capping. Dynamic light scattering revealed a hydrodynamic size of 255.8 nm with moderate colloidal stability (–25 mV zeta potential). SEM–EDX analysis further confirmed nanoscale morphology and high elemental purity of ZnO. Biological evaluation demonstrated concentration-dependent antibacterial activity, with maximum inhibition zones of 20 mm against *Bacillus* sp. and 15 mm against *Escherichia coli (E. coli)* at 1000 µg/mL. The antimicrobial efficacy is likely attributed to synergistic mechanisms including reactive oxygen species generation, Zn^{2+} ion release, and enhanced nanoparticle–membrane interactions facilitated by phytochemical surface functionalization. Collectively, these findings establish *Butea monosperma* root extract as a potent phytochemical reservoir for sustainable ZnO nanoparticle synthesis, offering a green, cost-effective, and biologically active nanomaterial platform. Future research should focus on detailed mechanistic investigations of antibacterial pathways, cytotoxicity assessment on mammalian cell lines to ensure biocompatibility, and surface engineering approaches to enhance functional performance. Additionally, scale-up optimization and application-driven studies in wound healing systems, antimicrobial coatings, and drug delivery platforms may significantly advance the translational and industrial potential of these biosynthesized nanomaterials.

Declarations

Ethical Approval

This study does not involve human participants or animals and therefore ethical approval was not required.

Consent to Participate

Not applicable.

Consent to Publish

All authors have read and approved the final manuscript and consent to its publication.

Author Contributions

RJ: Conceptualization, experimental investigation, data analysis, and manuscript writing.

SVM: Supervision, methodology validation, manuscript review and editing.

Funding

The authors received no specific funding for this work.

Competing Interests

The authors declare that they have no competing interests.

Availability of Data and Materials

All data generated or analysed during this study are included in this published article. Additional information can be provided by the corresponding author upon reasonable request.

ORCID iDs

Rajeshreeba A. Jadeja: - 0009-0002-2940-1820

Suranjana V. Mayani: - 0000-0002-2624-3305

References

[1] Oprea B, Martínez L, Román E, et al. Dispersion and functionalization of nanoparticles synthesized by gas aggregation source: opening new routes toward the fabrication of nanoparticles for biomedicine. *Langmuir* 2015; 31: 13813–13820.

[2] Makarov V V, Love AJ, Sinitsyna O V, et al. "Green" nanotechnologies: synthesis of metal nanoparticles using plants. *Acta Naturae (англоязычная версия)* 2014; 6: 35–44.

[3] Muehlethaler C, Leona M, Lombardi JR. Review of surface enhanced Raman scattering applications in forensic science. *Anal Chem* 2016; 88: 152–169.

[4] Jadoun S, Arif R, Jangid NK, et al. green synthesis of nanoparticles using plant extracts: A review. *Environ Chem Lett* 2021; 19: 355–374.

[5] Eustis S, El-Sayed MA. Why gold nanoparticles are more precious than pretty gold: noble metal surface plasmon resonance and its enhancement of the radiative and nonradiative properties of nanocrystals of different shapes. *Chem Soc Rev* 2006; 35: 209–217.

[6] Bello SA, Agunsoye JO, Hassan SB. Synthesis of coconut shell nanoparticles via a top-down approach: Assessment of milling duration on the particle sizes and morphologies of coconut shell nanoparticles. *Mater Lett* 2015; 159: 514–519.

[7] Faivre D, Bennet M. Magnetic nanoparticles line up. *Nature* 2016; 535: 235–236.

[8] Arakha M, Saleem M, Mallick BC, et al. The effects of interfacial potential on antimicrobial propensity of ZnO nanoparticle. *Sci Rep* 2015; 5: 9578.

[9] Diallo A, Ngom BD, Park E, et al. green synthesis of ZnO nanoparticles by Aspalathus linearis: structural & optical properties. *J Alloys Compd* 2015; 646: 425–430.

[10] Gross J, Sayle S, Karow AR, et al. Nanoparticle tracking analysis of particle size and concentration detection in suspensions of polymer and protein samples: Influence of experimental and data evaluation parameters. *European Journal of Pharmaceutics and Biopharmaceutics* 2016; 104: 30–41.

[11] Khlebtsov NG, Dykman LA. Optical properties and biomedical applications of plasmonic nanoparticles. *J Quant Spectrosc Radiat Transf* 2010; 111: 1–35.

[12] Comroe JH. The lung. *Sci Am* 1966; 214: 56–71.

[13] Handy RD, Von der Kammer F, Lead JR, et al. The ecotoxicology and chemistry of manufactured nanoparticles. *Ecotoxicology* 2008; 17: 287–314.

[14] Laurent S, Forge D, Port M, et al. Magnetic iron oxide nanoparticles: synthesis, stabilization, vectorization, physicochemical characterizations, and biological applications. *Chem Rev* 2008; 108: 2064–2110.

[15] Jain PK, Lee KS, El-Sayed IH, et al. Calculated absorption and scattering properties of gold nanoparticles of different size, shape, and composition: applications in biological imaging and biomedicine. *J Phys Chem B* 2006; 110: 7238–7248.

[16] Mirzadeh E, Akhbari K. Synthesis of nanomaterials with desirable morphologies from metal–organic frameworks for various applications. *CrystEngComm* 2016; 18: 7410–7424.

[17] Silva GA. Introduction to nanotechnology and its applications to medicine. *Surg Neurol* 2004; 61: 216–220.

[18] Pant HR, Pant B, Sharma RK, et al. Antibacterial and photocatalytic properties of Ag/TiO2/ZnO nano-flowers prepared by facile one-pot hydrothermal process. *Ceram Int* 2013; 39: 1503–1510.

[19] Mallakpour S, Sirous F. Surface coating of α-Al2O3 nanoparticles with poly (vinyl alcohol) as biocompatible coupling agent for improving properties of bio-active poly (amide-imide) based nanocomposites having l-phenylalanine linkages. *Prog Org Coat* 2015; 85: 138–145.

[20] Hajipour MJ, Fromm KM, Ashkarran AA, et al. Antibacterial properties of nanoparticles. *Trends Biotechnol* 2012; 30: 499–511.

[21] Nikalje AP. Nanotechnology and its applications in medicine. *Med chem* 2015; 5: 81–89.

[22] Parveen K, Banse V, Ledwani L. Green synthesis of nanoparticles: Their advantages and disadvantages. In: *AIP conference proceedings*. AIP Publishing LLC, 2016, p. 20048.

[23] Needham D, Arslanagic A, Glud K, et al. Bottom-up design of nanoparticles for anti-cancer diapeutics:"put the drug in the cancer's food". *J Drug Target* 2016; 24: 836–856.

[24] Qu Z, Liu P, Yang X, et al. Microstructure and characteristic of BiVO4 prepared under different pH values: photocatalytic efficiency and antibacterial activity. *Materials* 2016; 9: 129.

[25] Rogozea EA, Olteanu NL, Petcu AR, et al. Extension of optical properties of ZnO/SiO2 materials induced by incorporation of Au or NiO nanoparticles. *Opt Mater (Amst)* 2016; 56: 45–48.

[26] C Thomas S, Kumar Mishra P, Talegaonkar S. Ceramic nanoparticles: fabrication methods and applications in drug delivery. *Curr Pharm Des* 2015; 21: 6165–6188.

[27] Tratnyek PG, Johnson RL. Nanotechnologies for environmental cleanup. *Nano Today* 2006; 1: 44–48.

[28] Rogozea EA, Petcu AR, Olteanu NL, et al. Tandem adsorption-photodegradation activity induced by light on NiO-ZnO p–n couple modified silica nanomaterials. *Mater Sci Semicond Process* 2017; 57: 1–11.

[29] Puri A, Loomis K, Smith B, et al. Lipid-based nanoparticles as pharmaceutical drug carriers: from concepts to clinic. *Crit Rev Ther Drug Carrier Syst*; 26.

[30] Dablemont C, Lang P, Mangeney C, et al. FTIR and XPS study of Pt nanoparticle functionalization and interaction with alumina. *Langmuir* 2008; 24: 5832–5841.

[31] Torchynska T V, El Filali B, Ballardo Rodríguez IC, et al. Defect related emission of ZnO and ZnO Cu nanocrystals prepared by electrochemical method. *physica status solidi (c)* 2016; 13: 594–597.

[32] Yu ZB, Xie YP, Liu G, et al. Self-assembled CdS/Au/ZnO heterostructure induced by surface polar charges for efficient photocatalytic hydrogen evolution. *J Mater Chem A Mater* 2013; 1: 2773–2776.

[33] Wan D, Chen H-L, Lin Y-S, et al. Using spectroscopic ellipsometry to characterize and apply the optical constants of hollow gold nanoparticles. *ACS Nano* 2009; 3: 960–970.

[34] Yin Q, Wu W, Qiao R, et al. Glucose-assisted transformation of Ni-doped-ZnO@ carbon to a Ni-doped-ZnO@ void@ SiO 2 core–shell nanocomposite photocatalyst. *RSC Adv* 2016; 6: 38653–38661.

[35] Rawat MK, Jain A, Singh S. Studies on binary lipid matrix based solid lipid nanoparticles of repaglinide: in vitro and in vivo evaluation. *J Pharm Sci* 2011; 100: 2366–2378.

[36] Wang Y-C, Engelhard MH, Baer DR, et al. Quantifying the impact of nanoparticle coatings and nonuniformities on XPS analysis: gold/silver core–shell nanoparticles. *Anal Chem* 2016; 88: 3917–3925.

Figure Captions

Fig. 1 Graphical abstract illustrating the phytochemical-guided green synthesis of ZnO nanoparticles using *Butea monosperma* root extract and their antibacterial activity.

Fig. 2 HPLC chromatogram of *Butea monosperma* root extract showing polyphenolic compounds.

Fig. 3 LC–MS spectrum used for tentative identification of phytochemicals present in the extract.

Fig. 4 UV–Vis absorption spectrum and Tauc plot of biosynthesized ZnO nanoparticles indicating an optical band gap of 3.69 eV.

Fig. 5 FTIR spectrum of ZnO nanoparticles demonstrating functional groups involved in nanoparticle stabilization.

Fig. 6 SEM micrograph showing morphology of ZnO nanoparticles along with EDX spectrum confirming elemental composition.

Fig. 7 PXRD pattern of ZnO nanoparticles indicating hexagonal wurtzite crystal structure.

Fig. 8 Antibacterial activity of ZnO nanoparticles against *Escherichia coli (E. coli)* and *Bacillus* sp. using agar diffusion assay.

Fig. 9 Bar graph showing zone of inhibition of ZnO nanoparticles at different concentrations.

Supplementary Files

This is a list of supplementary files associated with this preprint. Click to download.

- SupplementryFileABAB.docx